

## APPENDIX A

### PUBLISHED DATA

| Experimenter      | specimen       | frequency     | velocity        | atten. coeff.       | modulus |
|-------------------|----------------|---------------|-----------------|---------------------|---------|
| Cecchi (1984)     | i.f. frog 4°C  | ≈ 4 kHz       | 167->208 m/s    | -                   | -       |
| Cecchi (1984)*    | i.f. frog      | ≈ 12 kHz      | 271 m/s         | -                   | -       |
| Blange (1985)     | s.f. frog 2°C  | .05 ms pulse  | 230 m/s         | -                   | various |
| Stienen (1985)    | s.f. frog 2°C  | .05 ms pulse  | 112 m/s (R)     | -                   | various |
| "                 | "              | "             | 230 m/s (A)     | -                   | various |
| Schoenberg (1974) | w.s. frog 6°C  | .8 m/s pulse  | 175 m/s (A)     | -                   | -       |
| "                 | "              | "             | 172 m/s (.87A)  | -                   | -       |
| "                 | "              | "             | 161 m/s (.5A)   | -                   | -       |
| "                 | "              | "             | 123 m/s (.14A)  | -                   | -       |
| "                 | "              | "             | ≈30 m/s (R)     | -                   | -       |
| "                 | f.b. frog 6°C  | "             | 169 m/s (A)     | -                   | -       |
| Hasan (1977)      | f.b. frog 5°C  | not specified | 51 m/s (R)      | -                   | 2.6 MPa |
| "                 | "              | "             | 175 m/s (A)     | -                   | 3.1 MPa |
| "                 | "              | "             | 144 m/s (RIGOR) | -                   | 2.1 MPa |
| Truong (1971)     | w.s. frog 25°C | 50 Hz         | 34 m/s (R)      | -                   | -       |
| "                 | w.s. frog 25°C | 10 kHz        | 142 m/s (R)     | -                   | -       |
| Truong (1974)     | w.s. frog 25°C | 3 kHz         | 60 m/s (R)      | frequency dependent |         |
| "                 | "              | 3 kHz         | 125 m/s (A)     | frequency dependent |         |
| Sadow (1947)**    | "              | not specified | 80 m/s (R)      | -                   | -       |

i.f. = intact single fibers

s.f. = skinned (permeabilized) fibers

f.b. = fiber bundles

w.s. = whole sartorius muscle

(R) = relaxed

(A) = fully activated, (.87A) = 87% activation, (.5A) = 50% activation, etc.

\*data are calculated from incidental data included in the discussion at the end of the paper.

\*\*reported in Truong (1978, page 1301)

**Table A.1.** The table lists the published data which includes strain wave or pulse propagation experiments for the measurement of muscle tissue viscoelasticity. Note that the above experiments often fail to include critical data on attenuation of the strain wave. For most of the pulse experiments, the frequency spectrum of the pulse was not calculated. It was assumed in these cases that the propagation velocity depended upon the "highest frequency components" of the pulse. Also, nearly all data of this type is limited to frog muscle specimens. No experiment included the effect of change of temperature. This is important because experimental temperatures often are not similar to physiologic temperatures, especially in mammalian single fiber experiments, and the effects of temperature on viscosity can not yet be discounted. Also, only one experimenter (Schoenberg) included the effect of partial levels of activation on pulse propagation velocity. In the published literature, the pulse propagation velocity is often not converted into an estimate of the elastic modulus.

## APPENDIX B

### TRIPLE NESTED-THREAD ACTUATORS

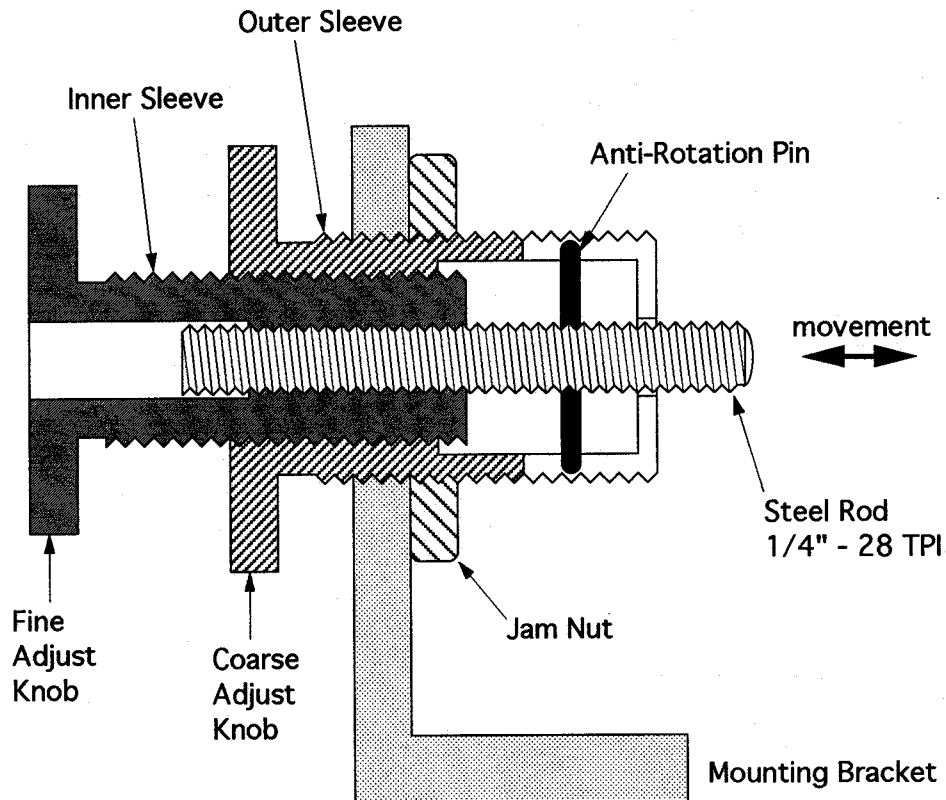


**Figure B.1.** Triple nested-thread actuators for precise positioning of the X-Y table. The inner sleeve internal thread is 1/4" - 28 TPI and the external thread is 1/2" - 20 TPI. The outer sleeve internal thread is 1/2" - 20 TPI and the external thread is 3/4" - 16 TPI. All threads are carefully cleaned and liberally greased with a high-viscosity lithium lubricant. The inner sleeve, outer sleeve, and jam nut are machined from 1 inch hexagonal stock, 70-30 brass. The threaded steel rod is type 304 stainless steel. The mounting bracket is machined from 2024 aluminum. The anti-rotation pin is a 1/16" x 1/2" tension pin forced through a hole in the threaded rod. Coarse position adjustments are made by loosening the jam nut and rotating the coarse adjust knob, resulting in a translation of 0.0625" (1.59 mm) per revolution. Fine position adjustments are made by tightening the jam nut against the mounting bracket and rotating the fine adjust knob. Relative rotation between the threaded steel rod and the outer sleeve is prevented by the anti-rotation pin, therefore rotation of the fine adjust knob results in a counter-rotation of the threaded rod internal to the inner sleeve. The translation resulting from rotation of the 1/2" - 20 TPI threads is counteracted by the 1/4" - 28 threads, resulting in a net movement of the steel rod of 0.0143" (363  $\mu$ m) per revolution.

## APPENDIX C

### SERVO MOTOR MODIFICATIONS

To apply high-frequency longitudinal strain pulses to the single muscle fibers, a commercially available moving-magnet scanner (Cambridge Technologies, Model 308) was modified. The rotary action of the scanner was transformed into linear reciprocal motion by a linearizing mechanism (Figure C.1). Moving magnet scanners of this type are often employed in muscle fiber mechanics research. A stainless steel tube is attached at the tip of the servo arm, perpendicular to the servo arm in the plane of rotation. The single muscle fiber is then connected to the end of the stainless tube, and fiber length is changed by commanding the servo to rotate. With a fixed arm arrangement such as this, the rotation of the servo produces not only a change in fiber length, but also a vertical movement of the end of the fiber which is attached to the extension tube. The vertical excursion is acceptable for low-speed muscle mechanics experiments, such as the determination of force deficit resulting from pliometric contractions, but the vertical excursion is unacceptable for high-speed sarcomere dynamics experiments, such as pulse propagation experiments.

The linearizer was tested to determine if high-frequency pulses would induce vibration of the trough at the end of the stainless steel tube. An optical displacement detector circuit was built (Figure C.2) which can detect displacements as small as 1  $\mu\text{m}$ . A brass rectangle, 0.102" x 0.150" x 0.002" thick, was affixed to a 29 ga. stainless steel tube, which was mounted to the moving plunger of a micrometer. The detector electronics were positioned so that the brass rectangle acted as an obstruction between the LEDs and the phototransistors. Lateral movement of the brass rectangle thus resulted in an increase in the light intensity striking one of the phototransistors, while decreasing the intensity of light striking the other phototransistor. The two output voltages from the two phototransistors were differentially amplified, and the output was calibrated in  $\mu\text{m}/\text{Volt}$ .

The thin brass rectangle was then affixed to the trough of the servo mechanism with wax. Once again, the detector electronics were positioned so that the brass rectangle acted as an obstruction between the LEDs and the phototransistors to detect lateral movement of the tip of the trough. The servo was operated over the full movement range to be used in the experiments, from the neutral position  $\pm 8^\circ$  of rotation of the scanner arm. Initially, the servo was operated very slowly to determine the baseline displacement. Once the baseline was established, the servo was commanded to perform full amplitude 1 kHz pulses in both directions. The lateral displacement during a rapid pulse as a function of servo position was subtracted from the baseline displacement using a digital storage oscilloscope (Gould DSO 475). The difference in lateral displacements was taken to be the displacement due to lateral vibration of the end of the servo trough. The thin brass rectangle was repositioned to detect vertical vibrations of the trough, and the above process was repeated to detect vertical vibrations of the trough when the servo performed rapid pulses.

The test results demonstrated that the servo trough lateral excursion was less than  $1 \mu\text{m}$  over the full range, and that no detectable vibrations were present when the servo was operated at high speed. The linearizer mechanism is not perfect, though it removes nearly all of the vertical movement of the trough over the normal range of operation (Figure C.1). The test demonstrated that the servo trough vertical displacement at each extreme position was  $\pm 7 \mu\text{m}$  from the neutral position. When this baseline displacement was subtracted from the vertical displacement of the trough during rapid pulses, no vibrations were detected. Therefore, although there is a small amount of vertical displacement as the servo is operated over the full range of displacements used in the pulse propagation experiments, no lateral or vertical vibrations of amplitude greater than  $1 \mu\text{m}$  were detected.

To take full advantage of the 8-bit resolution of the array controller (Appendix I), the control voltage input of the Cambridge servo motor controller were modified to

include three amplitude ranges. The array controller generated a  $\pm 10.0$  volt output voltage from each channel of the digital waveform synthesizer. Analog signal inputs to the array controller must be in the range of 0.0 to + 2.0 volts. The Cambridge servo motor controller does not include a position output signal, but the servo position can be determined by measuring the voltage on the controller board (Cambridge Technologies Part Number: CB6580) at TP1. The position voltage is  $\pm 5.1$  volts over the full range of movement of the servo. A circuit was designed and built to adapt this position voltage to the necessary range for the array controller analog-to-digital converters (Figure C.3).

The servo motor optimization circuit (Figure C.3) uses 12 adjustable resistors, each of which is a 25-turn ceramic potentiometer. The servo position input voltage from the array controller to the servo motor controller board is buffered by a BiFET op-amp voltage follower. The output from the buffer is divided into one of four ranges, and the desired output range is selected by single-pole, four position rotary switch (S1). S1 provides a control voltage for three analog multiplexers (74HC4066), allowing one of the four ranges to be selected. The four ranges are based on a fiber of 6 mm length, and allow a maximum pulse amplitude of 5%, 2%, or 0.5%, or full servo excursion. For all four ranges R4 (100 k $\Omega$ ) adjusts the servo input position offset. For the full excursion range R5 (5 k $\Omega$ ) adjusts the gain, and R12 (5 k $\Omega$ ) adjusts the output position offset. For the 5% range, R1 (10 k $\Omega$ ) adjusts the input divider, R6 (10 k $\Omega$ ) adjusts the gain, and R9 (5 k $\Omega$ ) adjusts the output position offset. For the 2% range, R2 (10 k $\Omega$ ) adjusts the input divider, R7 (50 k $\Omega$ ) adjusts the gain, and R10 (1 k $\Omega$ ) adjusts the output position offset. For the 0.5% range, R3 (1 k $\Omega$ ) adjusts the input divider, R8 (50 k $\Omega$ ) adjusts the gain, and R11 (1 k $\Omega$ ) adjusts the output position offset. The desired range is selected prior to each series of pulses and is recorded on the data sheet.

One additional modification was required to allow the servo range selection. The servo motor coil must be de-energized prior to switching the range because there is a transient loss of control signal each time the input position command signal source is

changed. If the servo coil were to remain energized, the result would be a violent position transient, which would damage the muscle fiber. To de-energize the servo coil, the + Motor wire on the Cambridge servo motor controller board was removed, and was replaced by a toggle switch. Prior to changing the servo range, the toggle switch is turned to the OFF position. By this means, servo position transients were eliminated from the system.

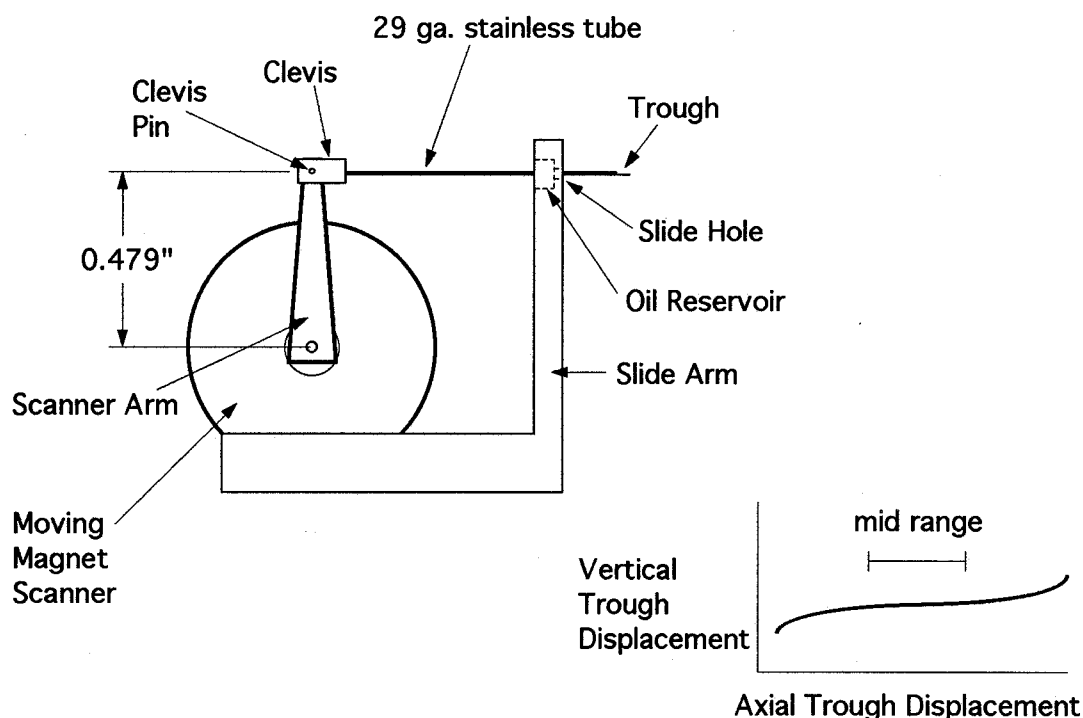


**Figure C.1.** Mechanical linearizer mechanism for the moving magnet scanner. The moving magnet scanner is a commercially available device (Cambridge Technologies, model 308). The clevis and slide arm are machined from 2024 aluminum plate. The clevis pin and trough are machined from 29 ga. thin-wall stainless tubing. The stainless steel tube with the trough is glued into a hole in the clevis, and passes through a slide hole in the slide arm. Concentric to the slide hole is an oil reservoir which is filled with low-viscosity sewing machine oil. This causes the stainless steel tube to be supported on a film of oil within the slide hole, thus reducing sliding friction to below 0.1 mN. The entire moving assembly of the linearizer mechanism has a mass below 50 mg to maximize the mechanical bandwidth and to prevent servo oscillations which result from excessive inertial load on the moving magnet scanner. The mechanism is illustrated at twice the actual size of the device. Movement of the tip of the trough is illustrated to the right of the drawing. At extreme rotations, the vertical movement of the trough becomes excessive, but for translations in the mid range, the vertical displacement never exceeds 20  $\mu\text{m}$ . All pulse propagation experiments were performed with translations in the mid range (center  $\pm$  20% of full scale) of the servo movement.

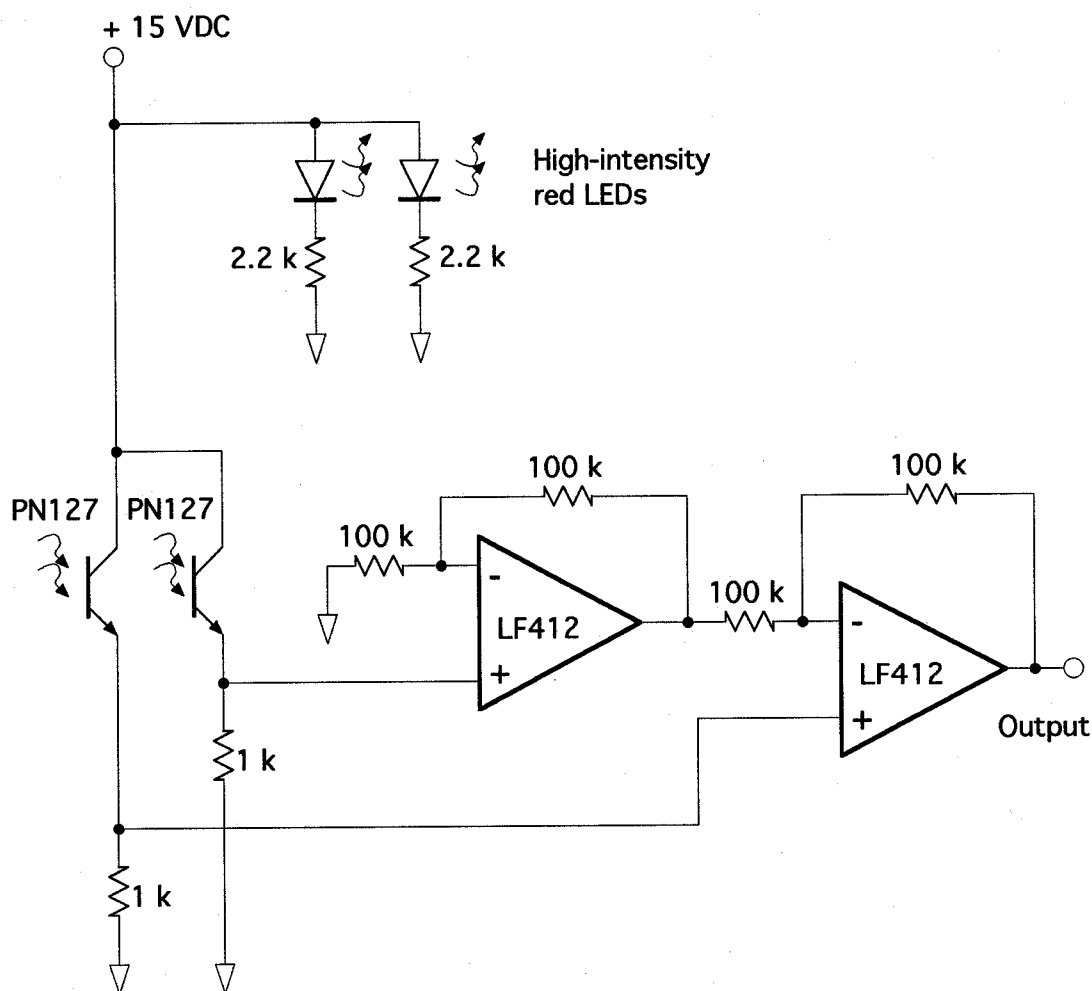


**Figure C.2.** Circuit diagram for the optical vibration detector. The amplifier employs two BiFET op amps in a simple high input impedance differential amplifier configuration. The op amp integrated circuits have  $0.1 \mu\text{F}$  decoupling capacitors from each power supply pin to ground (not shown). The PN127 phototransistors are clamped into a small fixture which holds them at a separation of  $0.100''$  center-to-center. The LEDs are clamped into a similar fixture and are located opposite the phototransistors, with a  $0.150''$  gap between each LED and its respective phototransistor.



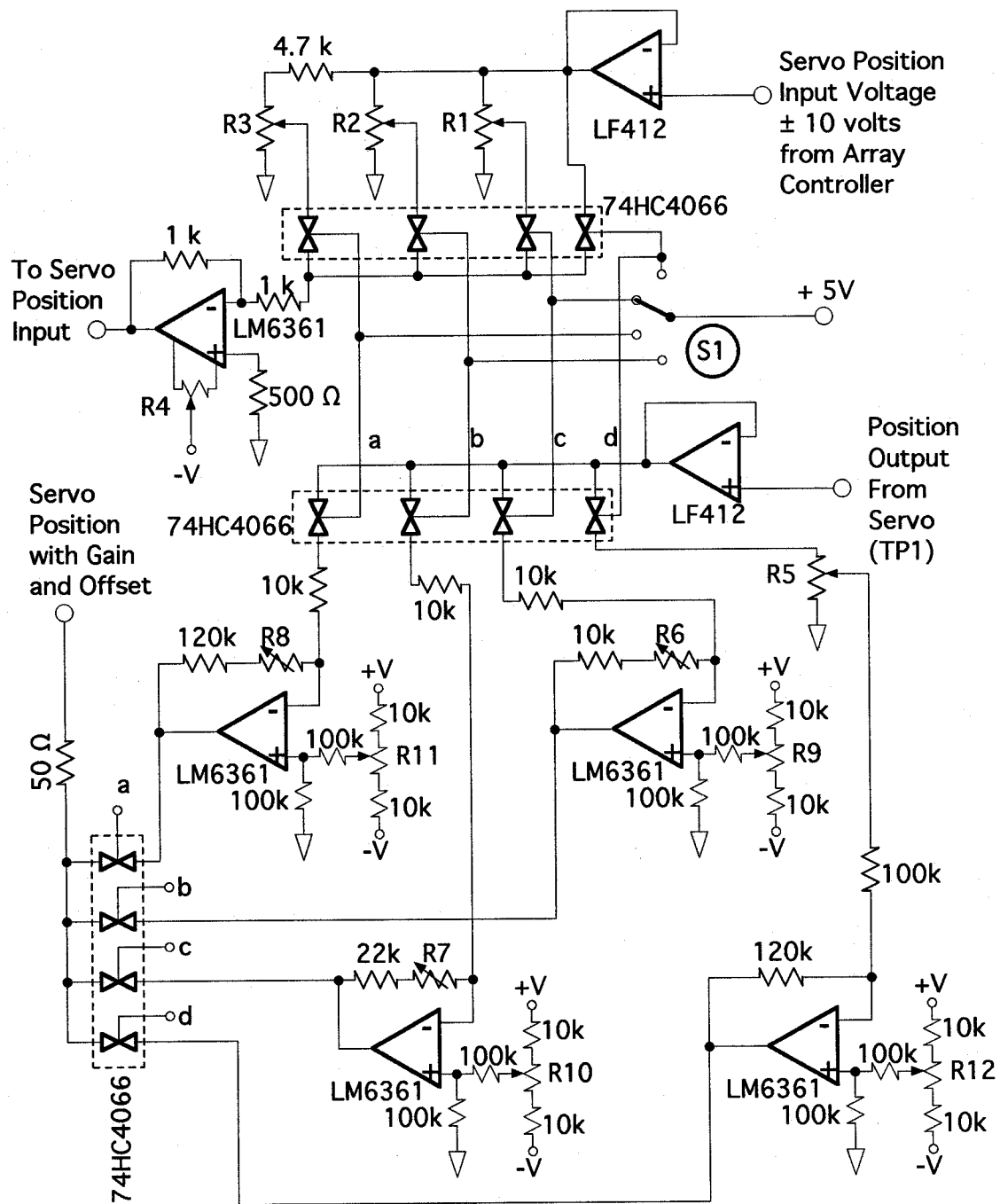


**Figure C.3.** Circuit diagram for the servo motor optimization circuit. All integrated circuits have 0.1  $\mu\text{F}$  decoupling capacitors from each power supply pin to ground (not shown). +V = positive 15 volts, regulated, and -V = negative 15 volts, regulated. The value and function of each of the adjustable resistors is given in the text. Control lines for the 74HC4066 analog multiplexers are connected in parallel as indicated by the lower case letters a, b, c, and d. Some of the control lines have been omitted for clarity.

## APPENDIX D

### PRECISION OPTICAL FORCE TRANSDUCER

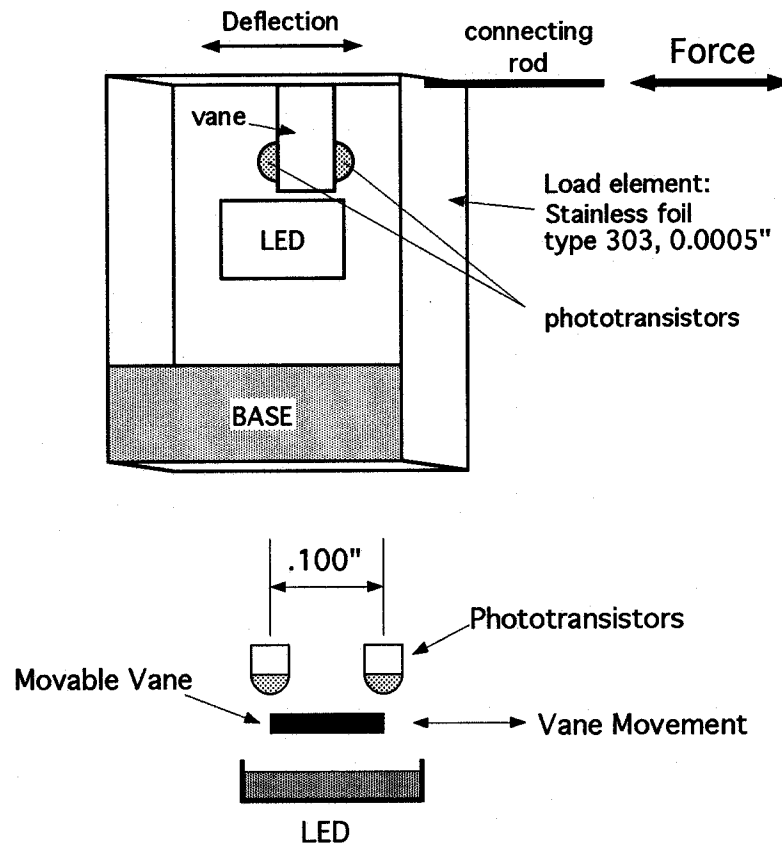


**Figure D.1.** Mechanical schematic of the precision optical force transducer. The load element is machined from a single sheet of stainless steel foil, which includes the vane, and is bent into the final shape before assembly. The vane is positioned between the LED and the phototransistors so that, in the neutral position (no load applied) the vane covers half of each phototransistor. Stainless steel foil up to .015" thickness has been found to work well with this general design, which permits force transducers with a full scale load capacity of up to 700 g to be built. Larger load ranges can be achieved if the load element is machined from metal plate, which, in principle, allows the load range to be increased to several tons. If the width of the load element is much larger than the thickness of the foil, the resulting force transducer is remarkably insensitive to off-axis loads. The use of small-area phototransistors reduces the full range linear deflection, which results in higher mechanical bandwidth and a more linear force-displacement curve for the device. Using 0.0005" thick stainless steel foil as a load element, the force transducer has a full scale displacement of 0.002" (51  $\mu\text{m}$ ) under a load of 1.20 mN. The undamped natural frequency is 350 Hz with a 29 ga. thin-wall stainless steel tube extension attached to the load element as the connecting rod. Using the amplifier electronics (Figure D.2.), the accuracy of the force transducer is  $\pm 0.002$  mN over the full range.

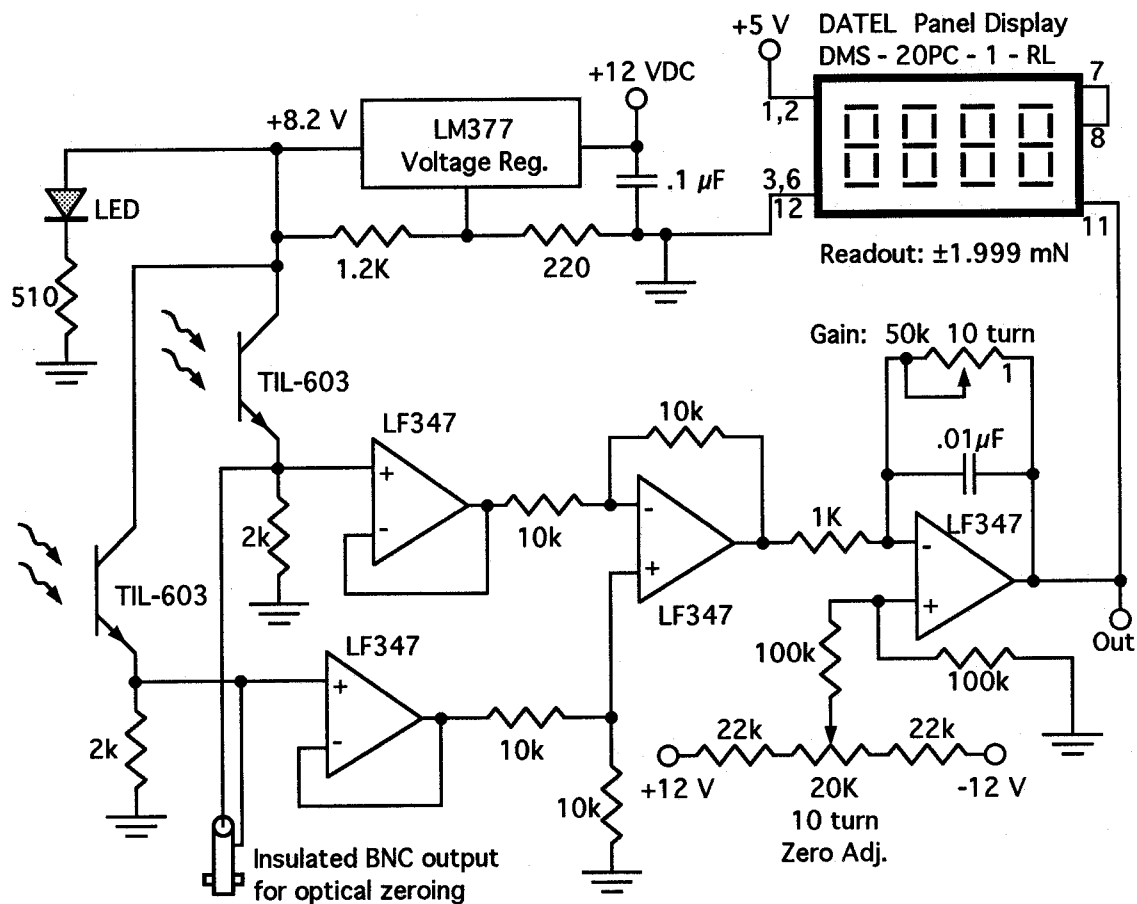


**Figure D.2.** Circuit diagram of the amplifier and display electronics for the precision optical force transducer. A surface-mount, high-intensity LED is used to illuminate two phototransistors (Texas Instruments TIL603). The stainless steel vane between the LED and the phototransistors moves in response to a mechanical load, causing an increased illumination on one phototransistor and a decreased illumination on the other phototransistor. The phototransistors are in emitter-follower configuration with 2 kΩ load resistors, and the resulting voltages from the two phototransistors are differentially amplified. In addition, the two phototransistor voltages may be accessed via a ground-isolated BNC lug which allows the force transducer to be mechanically centered, such that the steel vane is exactly in the center of the range of travel when no load is applied. The remainder of the electronics is provided to amplify and offset the differentially amplified phototransistor signal so that the resulting output is calibrated to 1 mV/μN. The force is displayed in real time to the nearest 1 μN on the DATEL digital panel meter.

## **APPENDIX E**

### **FLOW-THROUGH BATH DESIGN**

The level of activation of the single permeabilized muscle fiber is controlled by changing bath solutions in which the fiber is immersed. One method for changing the bath solutions is to use several baths, each containing a different solution, and to transfer the fiber from bath to bath. This design has the serious disadvantage that the fiber must be pulled through a fluid surface each time the fluid is to be changed. The surface tension of the bath fluid causes the fiber to be subjected to forces far in excess of the maximum isometric force that the fiber can generate when fully activated, therefore damage to the fiber is of concern. The problem of surface tension is exacerbated by the use of longer muscle fiber segments. The muscle fiber segments used in this series of experiments ranged in length from about 3 to about 7 mm, which is much longer than the 1 to 2 mm long fiber segments that are often used in single fiber experiments. In addition to the problem of pulling the fiber through surface tension, the removal of the fiber from the bath also requires that the top glass cover slip be removed and replaced each time the fiber is moved from one bath to another. No diffraction patterns can be taken while the top cover slip is removed, thus it is impossible to track the sarcomere dynamics in a single permeabilized muscle fiber during the process of activation if the fiber must be moved to a different bath.

An alternative for changing bath solutions is to withdraw fluid from the bath, until it is empty, then replace the fluid with the new solution. Though simple, this technique has the same disadvantages as the multiple bath design.

The best design employs a bath in which the fiber remains while fluid is simultaneously withdrawn and replaced with new fluid. The glass cover slip can remain in place and the fiber is not drawn through a fluid surface during this process. For this reason, a flow-through bath was designed into the apparatus for optical detection of pulse

propagation (Figure E.1). The bath is machined from type 304 stainless steel. The dimensions of the bath facilitate placement of 18 mm square cover slips both below and above the bath chamber. The bottom cover slip is glued into place with cyanoacrylate adhesive. The top cover slip is placed over the bath after the initial charge of relaxing solution has been added and the muscle fiber is in place. The surface tension of the bath fluid, which is initially filled to slightly over full, will pull the top cover slip into place because of the surface tension of the bath fluid. The cover slip tends to self-center because of the symmetry of the stainless steel bath housing.

Fluid is introduced into the bath through one of the 18 ga. stainless steel tubes (Figure E.1), while simultaneously being withdrawn through the other tube. The volume of the fluid in the bath remains constant during the exchange because equal volumes of fluid are added and removed simultaneously. This is accomplished by a simple fixture in which two 5 cc syringes are clamped anti-parallel. Each syringe is connected to one of the 18 ga. stainless steel tubes on the bath by a short length of 0.040" ID Tygon tubing. One of the syringes is filled with the new solution, while the other is empty. As the fluid is discharged from the first syringe, the second syringe withdraws an equal amount of fluid from the bath.

The fluid is injected into and withdrawn from the bath at opposite ends, and at an angle perpendicular to the long axis of the bath chamber. This causes very good mixing of the bath fluid during exchanges. Because the volume of the bath is known to be 0.4 cc, and because the fluid is being exchanged isovolumetrically, it is possible to calculate the volume of fluid exchange required to achieve any desired level of new fluid purity after the exchange. Defining  $V$  as the bath volume,  $Q$  as the total transfer volume of fluid,  $m$  as the effective volume of new solution in the bath after any volumetric exchange  $Q$ , and assuming that the new fluid is 100% pure before injection into the bath, we define the purity of the fluid in the bath after the exchange as:

$$P = \frac{m}{V} \quad \text{Eq. E.1}$$

The rate at which the old solution is replaced by the new can be expressed as:

$$\frac{dm}{dQ} = Q - \frac{m}{V} Q \quad \text{Eq. E.2}$$

This first-order differential equation is easily solved by rearranging and integrating to obtain:

$$-V \ln \left( 1 - \frac{m}{V} \right) = \frac{1}{2} Q^2 + C \quad \text{Eq. E.3}$$

The initial condition of the bath is that the bath contains no new fluid before the exchange, thus  $m(0) = 0$ , and therefore the arbitrary constant  $C$  is zero. Solving for  $Q$  and substituting from Eq. E.1 yields:

$$Q = \sqrt{-2V \ln(1 - P)} \quad \text{Eq. E.4}$$

The bath volume,  $V$ , is 0.4 cc from the geometry of Figure E.1. The exchange volume  $Q$  is then calculated directly from the desired bath fluid purity,  $P$ . For a desired purity of 99.9% new fluid in the bath after the fluid exchange,  $P = 0.999$ , and the required exchange volume is 2.35 cc. To compensate for the fact that there may not be perfect mixing within the bath, and the fact that some of the original bath fluid may be reintroduced into the bath after the exchange because it was trapped between the top cover slip and the stainless steel bath housing, the total exchange volume is doubled, for a

safety factor of 2 in the design. The resulting total exchange volume is 4.7 cc to assure 99.9% fluid purity after the exchange. For this reason, 5 cc syringes are used for exchanging the bath fluid.

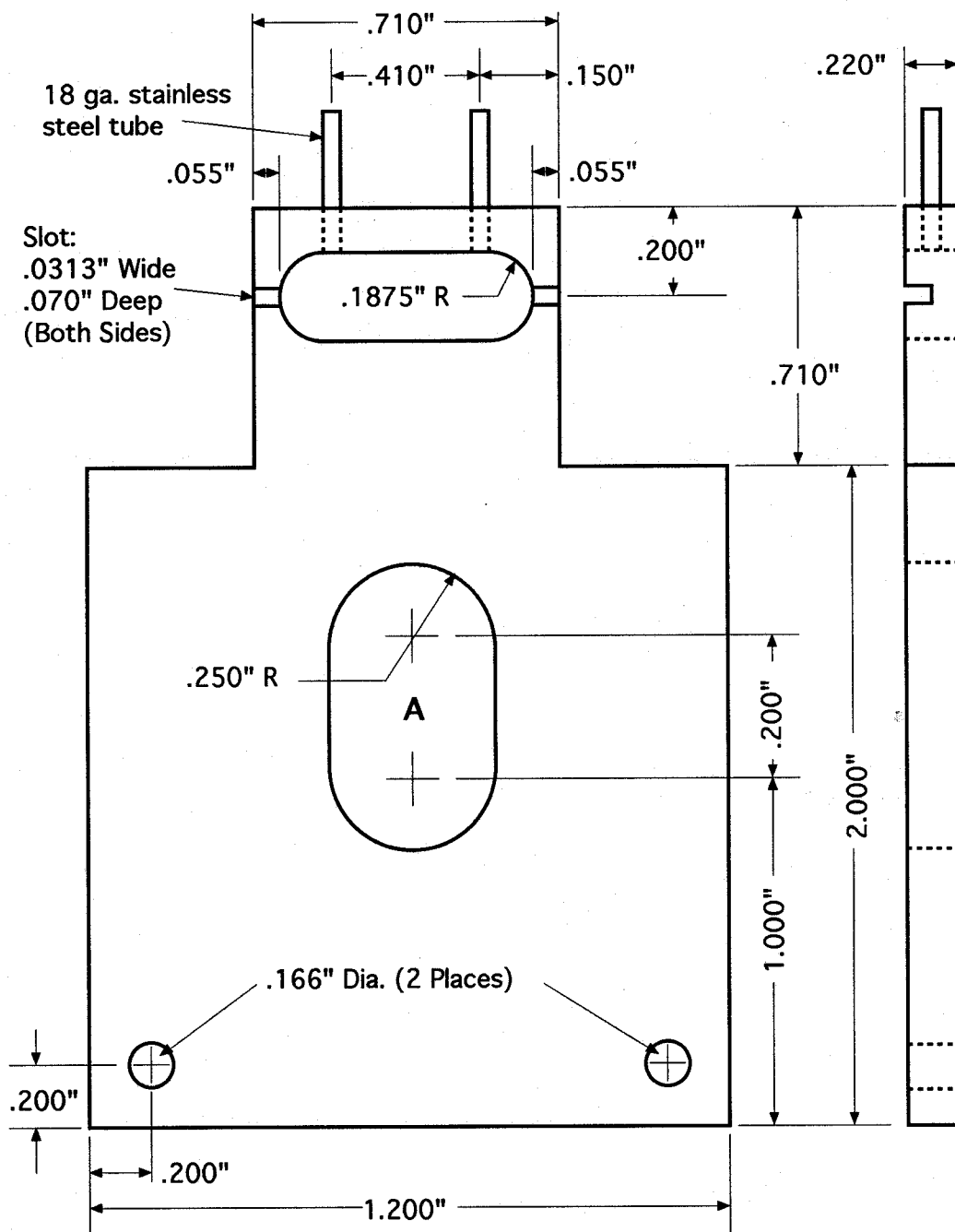


**Figure E.1.** Flow-through bath design. The drawing is not to scale. The bath is machined from type 304 stainless steel. Fluid is exchanged through the two 18 ga. stainless steel tubes, which are glued into place using cyanoacrylate adhesive. The bath chamber volume is 0.4 cc. The large slot (A) in the center of the bath plate is for the LM35D CMOS temperature transducer. The 0.166" diameter holes are for mounting the bath plate to the X-Y table of the experimental apparatus.



## APPENDIX F

### MEASUREMENT OF COHERENCE LENGTH

In order to test the hypothesis that the steps and pauses in the sarcomere length vs. time traces are due to interference of scattered light with the diffracted light (Burton and Huxley, 1995) a diode laser with a very short coherence length was used in the experimental apparatus as well as a He-Ne laser. Burton and Huxley have argued that the steps and pauses in the sarcomere length pattern are due to interference between the diffraction pattern arising from the regular sarcomere spacing and scattered laser light. They demonstrate their hypothesis by showing the effect on the centroid of the diffraction pattern when small particles or a glass surface is placed at various distances from the single fiber. The minimum distance tested was 100 microns from the fiber; shorter distances ran the risk of mechanical interference. Goldman (1987) has done experiments with laser light of reduced coherence, thereby reducing the amplitude of the steps and pauses.

The light from a diode laser ( $\lambda = 670$  nm, 4.2 mW, Applied Laser Systems # VLM 2-5C(L)) was unknown, so it needed to be measured (Yariv, page 386 ff.). A Michelson interferometer was constructed to measure the coherence length (Hecht, 1990). The method involved the movement of one of the two mirrors of the interferometer until it was no longer possible to detect interference fringes at both ends of the range over which interference fringes were visible. The supply voltage was varied over the full operational range of the laser diode module, and the results are tabulated below:

| <u>Volts</u> | <u><math>\Delta x_c</math> (microns)</u> |
|--------------|--|
| 4.89         | 305                                      |
| 5.04         | 330                                      |
| 6.00         | 2794                                     |
| 7.00         | 3886                                     |

|      |        |
|------|--------|
| 8.00 | > 4000 |
| 9.00 | 838    |
| 9.49 | 305    |

It is clear from the above table that the coherence length of the laser diode module is highly dependent upon the supply voltage. This convenient fact allows the laser light coherence length to be controlled over a limited range by varying the supply voltage. For these experiments, the supply voltage was set to a stable + 4.90 volts to minimize the coherence length and thus minimize the probability of interference with light scattered from sources in the optical path other than the single fiber.

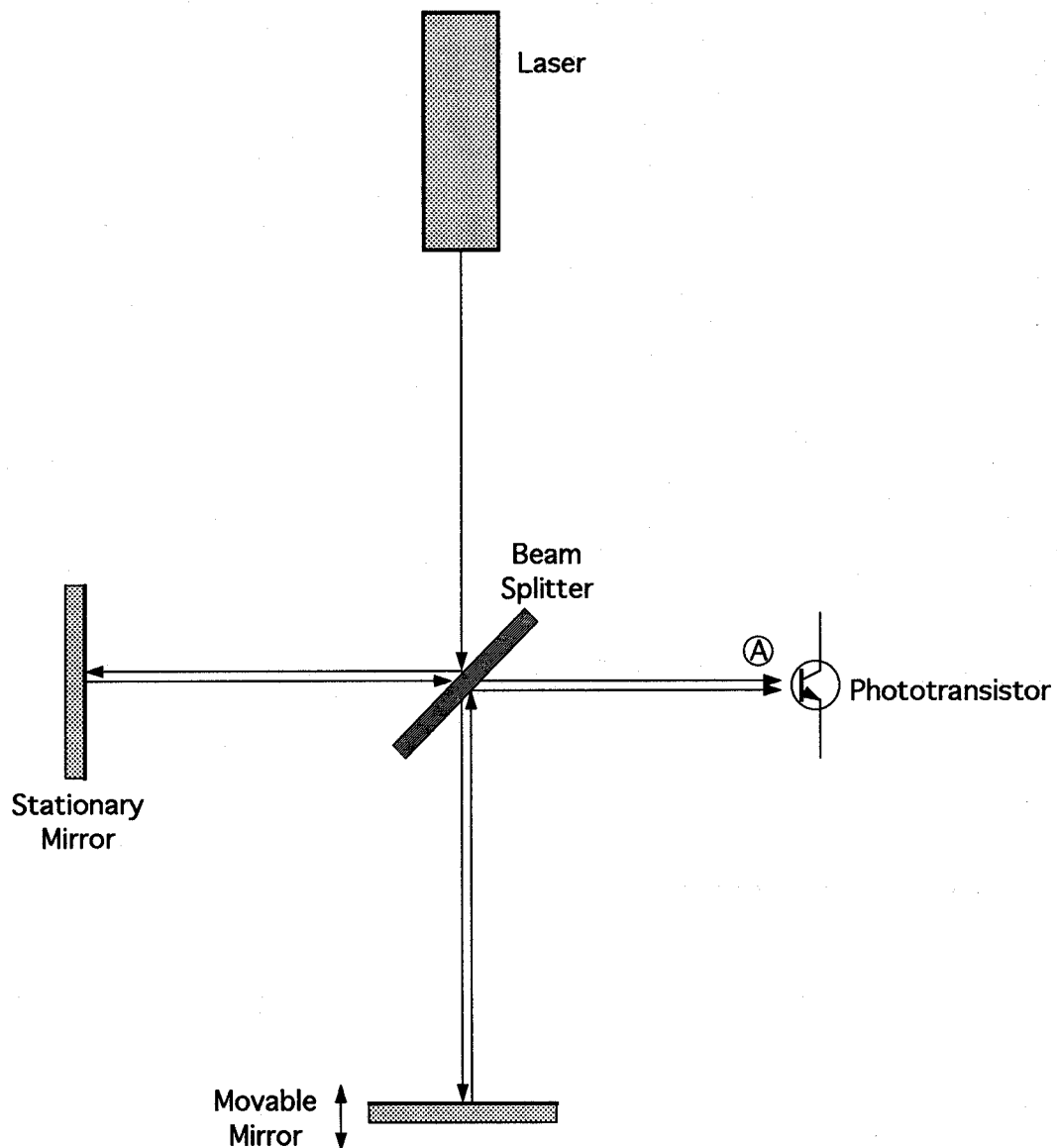


**Figure F.1.** A Michelson interferometer was used to measure the coherence length of the laser light from both a Helium-Neon laser ( $\lambda = 632.8 \text{ nm}$ ,  $10 \text{ mW}$ ) and a diode laser module ( $\lambda = 670 \text{ nm}$ ,  $4.2 \text{ mW}$ ). The beam is split and reflected from two separate mirrors as shown. One of the mirrors is moved a variable distance to shorten or lengthen one of the optical paths. The beams are then recombined and an interference pattern is generated, provided the difference in light path lengths does not exceed the coherence length of the laser light. When properly aligned, a bullseye-like pattern of bright and dark concentric circles of light appears at A. The phototransistor is placed in the center of this pattern. Displacement of the movable mirror causes the bullseye pattern to alternate from light to dark in the center, which is detected by the phototransistor.

## **APPENDIX G**

### **MAINTENANCE RAMP GENERATOR CIRCUIT**

A maintenance ramp generator circuit was designed and built to provide a signal for the servo motor. A periodic shortening ramp is used for maintaining sarcomere length homogeneity and muscle fiber viability when the fiber is activated (Brenner, 1983). The circuit (Figure G.4) allows user selectable inputs for ramp speed in fiber lengths per second (S1), Run or Hold mode (S2), time interval between ramps in seconds (S3), ramp amplitude in mm (S4), and servo position offset in mm (S5). Single-turn potentiometers are used at S1, S3, S4 and S5, and are calibrated directly in the desired units. Before calibration of this circuit, the servo motor calibration must be known.

The potentiometer values in this circuit can be modified to allow the circuit to be used with any Cambridge-type servo motor system. The ramp output is summed with other servo control voltages, such as that generated by the array controller digital waveform synthesizer, prior to connection to the position input for the servo motor.

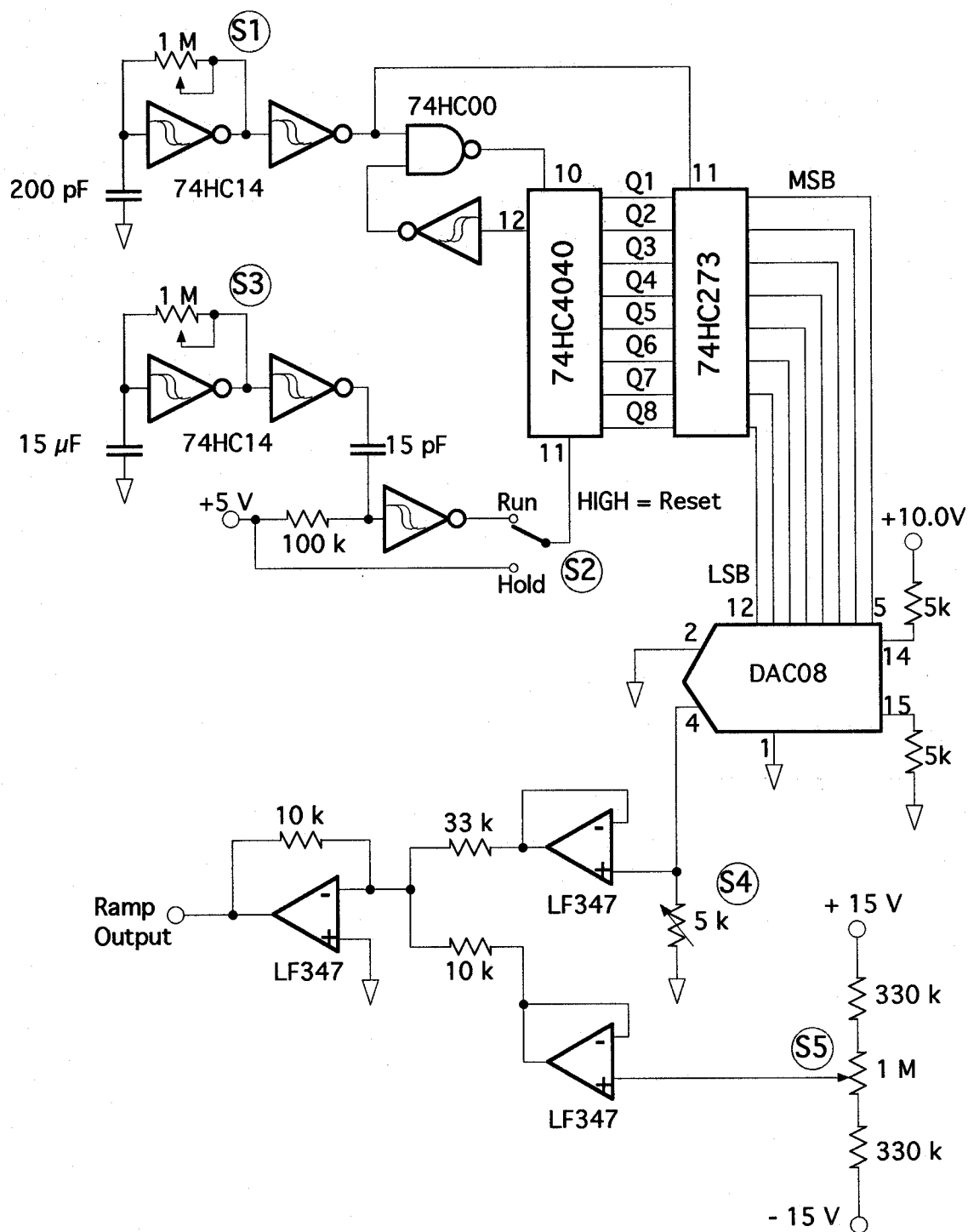


**Figure G.1.** Circuit diagram for the ramp function generator. All integrated circuits have 0.1  $\mu\text{F}$  decoupling capacitors from each power supply pin to ground (not shown). The functions of each switch and potentiometer are as follows: S1 controls the ramp speed, S2 sets the circuit to generate ramps (Run) or hold, S3 sets the interval between ramps, S4 sets the amplitude of each ramp, and S5 allows the servo position offset adjustment.

## **APPENDIX H**

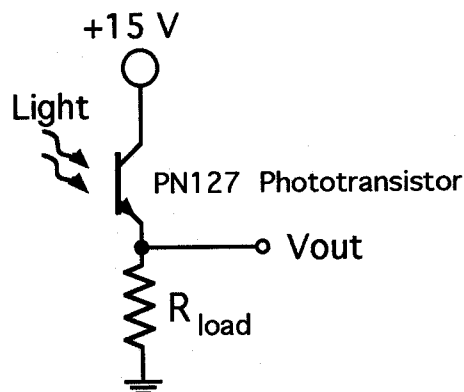
### **PHOTOTRANSISTOR ARRAY CONFIGURATION**

The detector head was constructed using fast phototransistors (Panasonic # PN127) in emitter-follower configuration with a  $470\ \Omega$  load resistor (Figure H.1). This simple configuration allowed parallel construction of the detector array with a minimum of components because no preamplification was necessary.

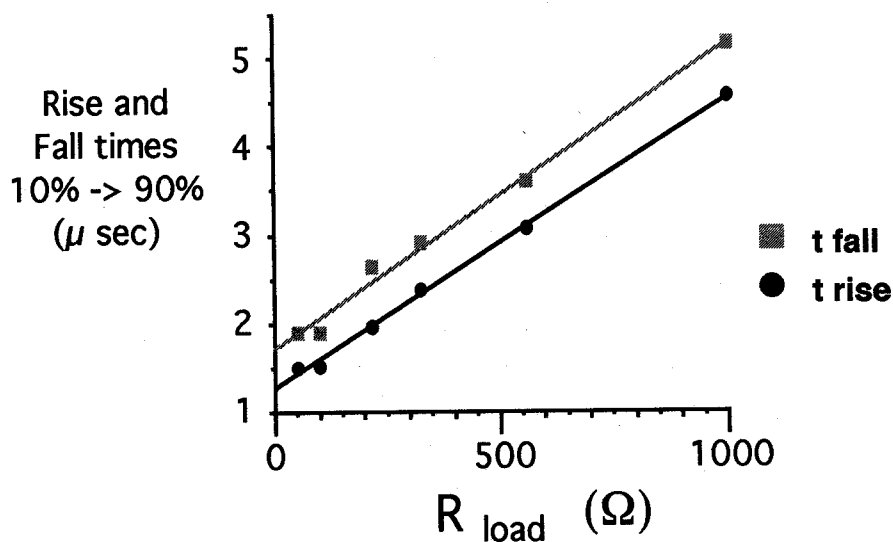
The full scale signal for the analog to digital converters is 0.0 to + 2.0 volts, and therefore this range was defined as the large signal amplitude for the rise and fall times of the phototransistors (Figure H.1). For the first-order diffraction patterns, the signal rarely exceeded half of this value, so 0.0 to + 1.0 volts was considered the upper limit for small signal response of the phototransistors. The small signal rise and fall times were approximately half that for the large signal rise and fall times, thus a  $470\ \Omega$  load resistor results in a small signal response delay of, at maximum,  $2\ \mu\text{s}$ . The detector array was therefore capable of collecting data at up to 500 kS/sec, with the phototransistors as the speed-limiting component of the system.

The phototransistors were clamped into an aluminum fixture which aligns all 64 phototransistors and fixes the center-to-center spacing to 2.21 mm. The aluminum fixture also houses the load resistors. The assembly of the aluminum fixture, phototransistor array, and load resistors comprise the detector head, which is detachable from the array controller and may be easily replaced or modified.

(a) Electrical configuration



(b) Large-signal rise and fall times ( 10%  $\rightarrow$  90% )



(c) Phototransistor array geometry

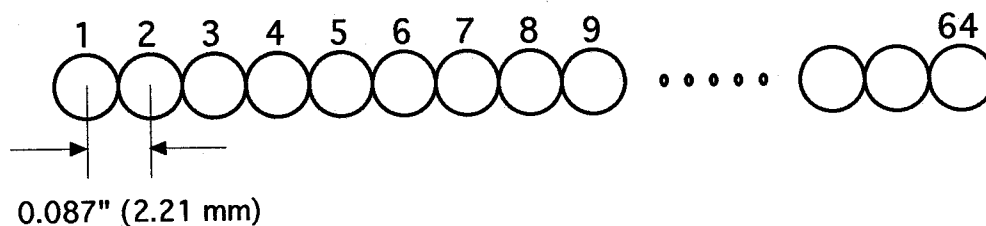


**Figure H.1.** Phototransistor characteristics and configuration. The phototransistors are each in emitter-follower configuration (a) with a load resistance of 470  $\Omega$ . The 0.0 to + 2.0 volt rise and fall times (b) were determined for a 10% to 90% signal response time. Small signal (less than 1.0 volt) rise and fall times are approximately twice as fast as the large signal times. The 64 phototransistors are clamped into an aluminum fixture which defines the detector array geometry (c).

## APPENDIX I

### ARRAY CONTROLLER

The central feature of the experimental setup for the optical measurement of pulse propagation in single permeabilized skeletal muscle fibers is the data acquisition system. The system is constructed with a totally parallel architecture to collect diffraction spectra rapidly enough and in large enough numbers for a complete record of the pulse propagation between two points on a fiber to be generated. The data acquisition system was designed specifically for this series of experiments, and is referred to as the *array controller*.

The array controller has a 64 channel parallel analog-to-digital converter system, with dedicated SRAM for each channel. The converter channels are assembled in groups of four. The group of four analog-to-digital converters, each with its dedicated SRAM and the support electronics, is designated as one ADC/M board, and is shown schematically in Figure I.1. A 64-to-1 demultiplexer (Figure I.2) is included in the control electronics for downloading the SRAM to microcomputer for processing.

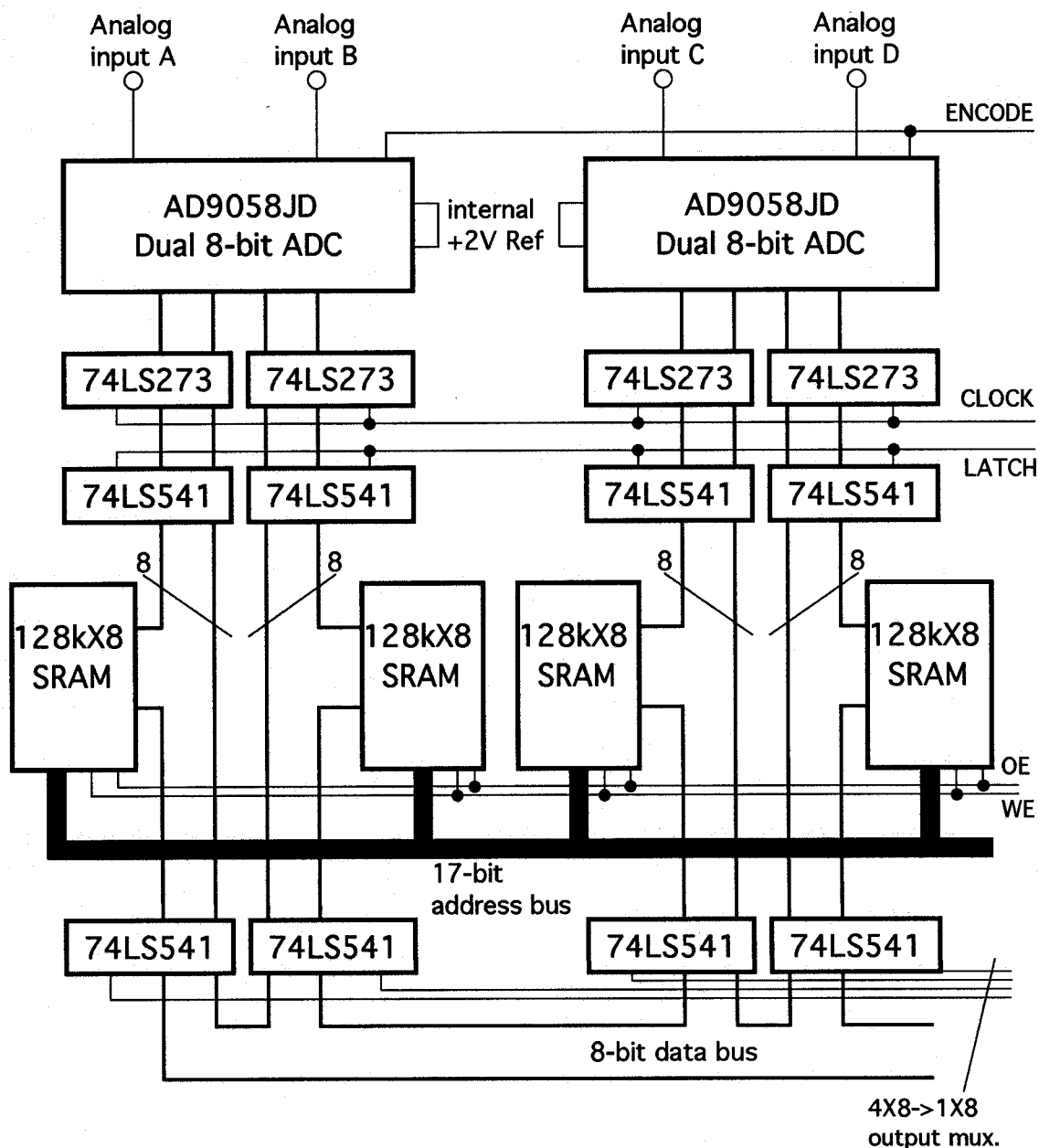
All analog-to-digital conversions are clocked in parallel by an ENCODE signal which is generated by a precision quartz oscillator (Figure I.3). The quartz oscillators are located on the clock/address driver board, which also generates all control signals for the entire system, such as the SRAM address and read/write enable. The clock speed of the system is set by selecting one of 6 quartz oscillators and one of 8 divider settings. The memory is divided into 1, 2, 4, 8, 16, 32, 64, or 128 sectors for individual experiments by counting in parallel with address bit 9 and disabling the clock when the count value reaches the desired value (Figure I.3). Sampling resumes when the counter is reset to zero, either from the local control panel or from the computer.

Four digital waveform synthesizers (Figure I.4) are included in the system to generate analog signals for controlling servo position and other external devices during

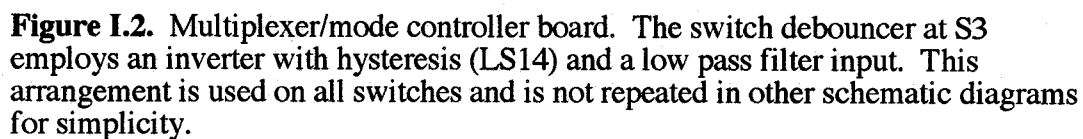


the execution of the experiment. Each digital waveform synthesizer has 8-bit resolution and is hard-wired to a specific output voltage range as appropriate for the device for which it will be generating control signals. All four digital waveform synthesizers are located on one board, designated the DAC board. The DAC board and all ADC/M boards are clocked in parallel and access the same address bus. The timing diagrams are provided in Figure I.5.

The system is configured prior to each experiment at the local control panel (Figure I.6) which is mounted to the top of the array controller. The operational mode, memory block size, clock speed and divider must be selected on this control panel prior to each set of experiments. Each experiment is initiated from either the local control panel or from the computer key board. Data transfer between the computer and the array controller is accomplished via a 24-bit digital I/O board (National Instruments DIO-24). The computer generates 8-bit files which are downloaded to the array controller to program the digital waveform synthesizers. After completion of a full battery of experiments, the computer generates pulses to advance the memory address counter (Figure I.3) and 64-to-1 multiplexer (Figure I.2) to serially download the converted 8-bit values from the SRAM on the ADC/M boards into the microcomputer memory for analysis and storage.



**Figure I.1.** Analog-to-digital and memory (ADC/M) board schematic. Four analog-to-digital converter channels are located on each ADC/M board. All control voltages are generated by control electronics located on the clock/address driver board (Figure I.3). Voltage references are internal to each of the analog-to-digital converters.



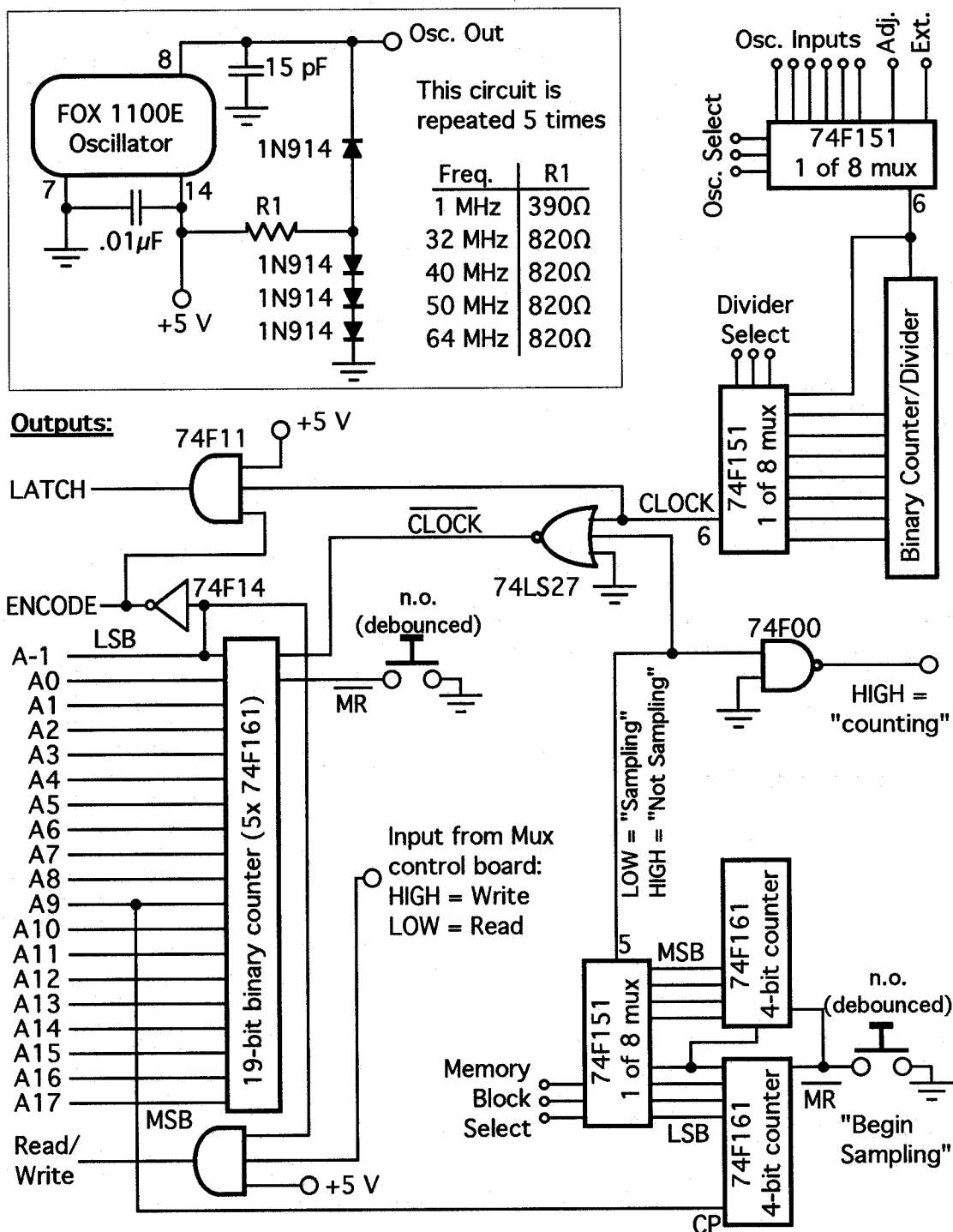


**Figure I.3.** Clock/Address driver board. This circuit provides a cold-switched, selectable quartz oscillator clock, clock divider, as well as an address counter and drivers for all SRAM memory chips in the Array Controller. The oscillator, divider, and memory block size are selected by multiplexers as shown. This circuit also generates read/write control values for the Array Controller memory chips, and the LATCH and ENCODE pulses. The sampling rate of the system =  $\text{CLOCK}/2$ .

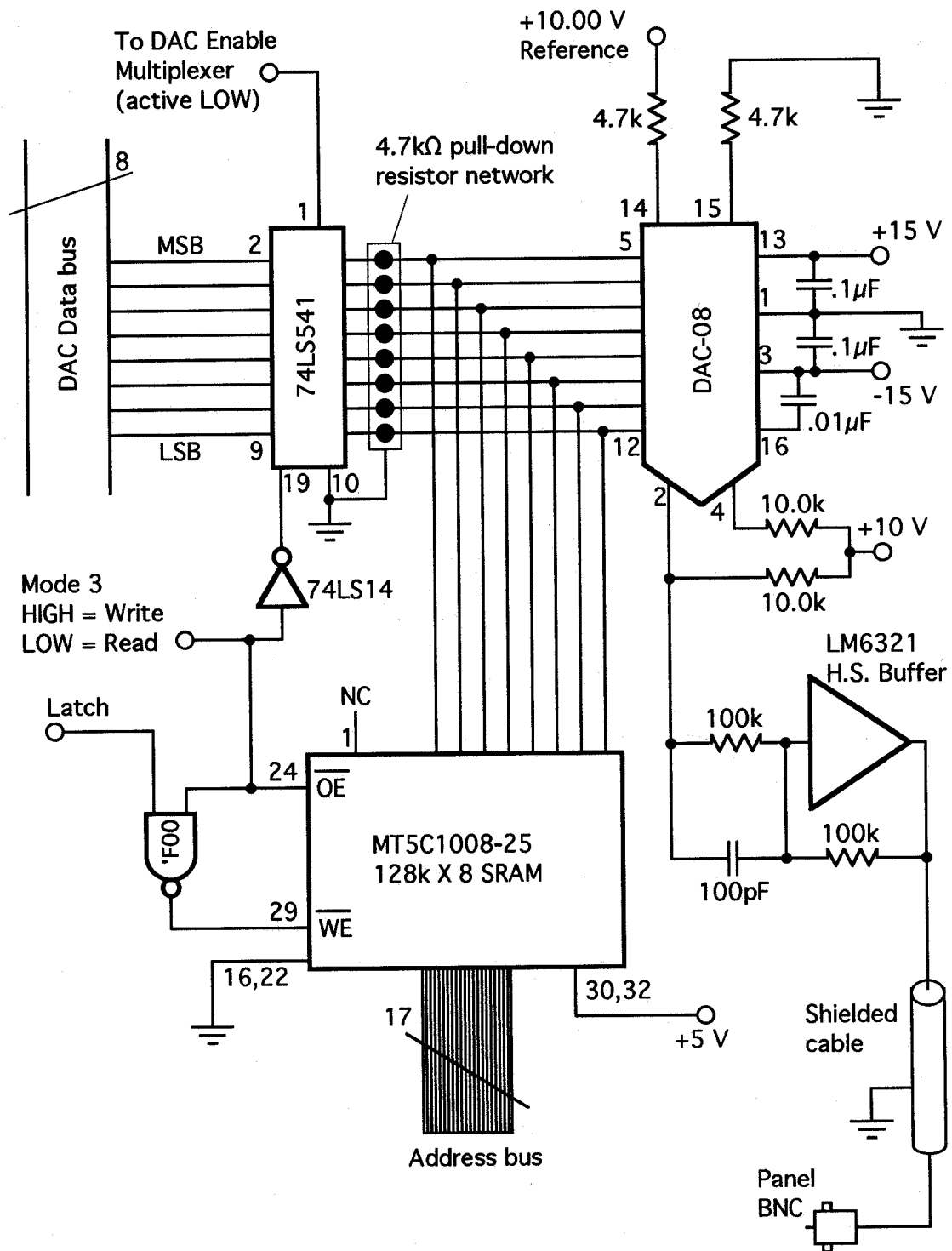


**Figure I.4.** Digital Waveform Synthesizer board schematic. This circuit is duplicated 4 times, once for each digital waveform synthesizer channel. Output voltage swing is  $\pm 10.0$  Volts.

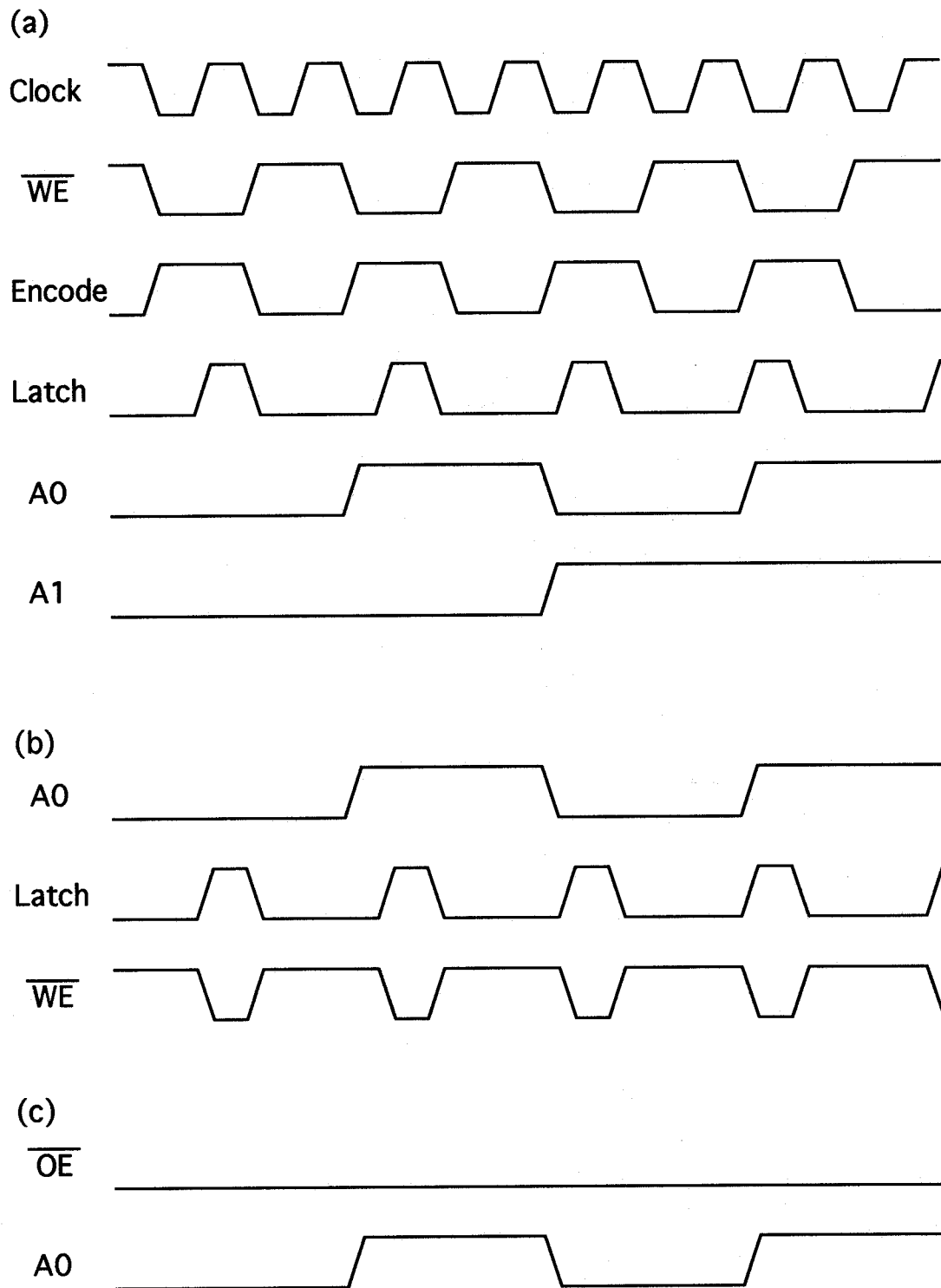
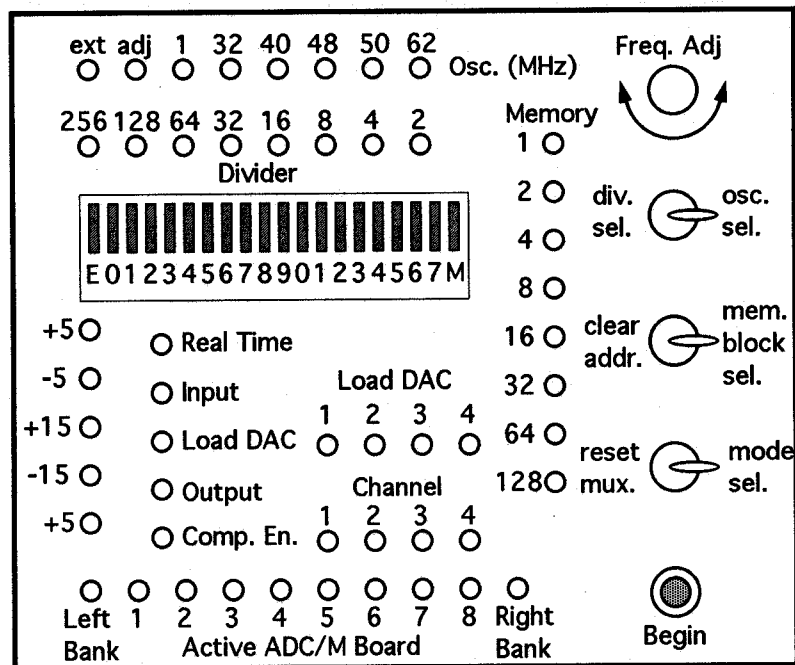


**Figure I.5.** Timing diagrams for the Array Controller. (a) Timing of the analog-to-digital converter boards. (b) Timing of the write cycle for the digital waveform synthesizer memory. (c) Read cycle for the digital waveform synthesizer memory.



| D-SUB<br>DIO Pin# | Description                 |
|-------------------|-----------------------------|
| 1                 | Load DAC (Bit 0)            |
| 2                 | Load DAC (Bit 1)            |
| 3                 | Begin Sampling (Pulse HIGH) |
| 4                 | N.C.                        |
| 5                 | Advance Address Counter     |
| 6                 | Advance Channel Mux         |
| 7                 | Reset Channel Mux           |
| 8                 | Disable/Enable Fans         |
| 9                 | Input (MSB)                 |
| .                 | .                           |
| .                 | .                           |
| .                 | .                           |
| 16                | Input (LSB)                 |
| 17                | DAC Output (MSB)            |
| .                 | .                           |
| .                 | .                           |
| .                 | .                           |
| 24                | DAC Output (LSB)            |
| 25                | GROUND                      |

**Figure I.6.** Control panel and Digital I/O cable configuration. The experiments can be executed remotely using the computer, but it is necessary to set the experimental parameters, such as oscillator, clock divider, and memory partitioning, on the control panel of the Array Controller.

## **APPENDIX J**

### **COMPUTER PROGRAMS**

The experimental control, data collection, data analysis, and data file handling for this research required special programs to be written. The programming language chosen was VisualBASIC for DOS v1.0 (Microsoft). This language was chosen because of its transportability between IBM compatible machines, the ease with which programs can be developed, and modified, and the fact that the digital I/O board that was chosen for interfacing the computer with the Array Controller was supplied with software to support VisualBASIC for DOS. In total, approximately 200 pages of code were written to carry out all computer-related functions of this research. Descriptions each program and the relevant algorithms follow.

#### **TILT NORM.BAS**

This program automatically calculates the optical geometry for the setup based on physical measurements of known reference points on the experimental setup and the Array Controller. The program assumes normal incidence of the laser beam on the muscle fiber. Normal incidence of the beam is set and checked to within  $0.5^\circ$  during setup of the experimental apparatus. The program accounts for many variables particular to the instrumentation that was built for this series of experiments; for example, it accounts for the sensitivity half-angle of the photodiodes and allows the phototransistor array to be placed at such an orientation that the maximum response will be elicited for diffracted beams within the expected range of diffraction angles. The program uses the geometrical reference point values to calculate the maximum and minimum diffraction angles that can be detected, dimensional constants to be used by later programs to transform the spectral data into sarcomere lengths, and estimated resolution of sarcomere length for various diffraction angles.



The program also indicates the diffraction angle and sarcomere length at which the diffracted beam is normally incident upon the phototransistor array to allow for compensation of intensity loss due to non-normal incidence on the phototransistor at different diffraction angles. Because the 50% sensitivity half-angle of the phototransistors (Panasonic PN127) is  $13^\circ$ , and because the range of sarcomere lengths studied in these experiments allow diffraction angles of  $8.3^\circ$  to  $21.9^\circ$  for the first order diffraction peak (using a He-Ne laser at 632.8 nm wavelength), the differing incidence angles would distort the calculated diffraction peak centroid because of the reduction of the apparent intensity of the diffracted light at angles of incidence on the diode array that deviate further from normal incidence. The result would be a tendency to underestimate sarcomere length pulse amplitudes that are detected at diffraction angles above and below the diffraction angle at which the light is incident on the phototransistor array. This program supplies the necessary information to the other programs to allow this effect to be compensated for.

The output from this program is stored in a data file (TILTNORM.DAT) that is accessed by other programs, and the results are displayed to allow optical geometries for the experimental setup to be developed and optimized for each type of experiment.

### **DACFMAKR.BAS**

This program allows the user to create data files that will be used to load the memory for the 8-bit digital wave form synthesizers that are built into the Diode Array Controller. The data files are comma delimited 8-bit integers and are designated as xxxxxxxx.DAC. These wave forms may be used to automatically control experimental variables that are too fast to be controlled by normal computer I/O. For example, the wave forms used in this series of experiments provide voltages to control the servo motor motion during each experiment. The program allows up to four digital channels to be programmed. The program can generate ramps, steps, square waves or short pulses of

any desired initial baseline, period, slew rate or amplitude. In addition, the program can combine steps with ramps and partial sinusoids to allow a very wide variety of synthesized wave forms to be generated. This capability is important because although this series of experiments only requires control of servo motor position, in future experiments wave forms will be generated to control laser beam deflection using an acusto-optic modulator, laser pulses to release caged molecules, electrodes to stimulate intact single fibers and other events that must be rapidly controlled or initiated at well-defined points in time during an experiment.

### **LOADDAC.BAS**

This program allows the user to select the desired digital wave form file for a set of experiments. Once the file has been selected, this program automatically loads the digital values into the memory of the digital wave form synthesizer channels in the Diode Array Controller. When this function is complete, the program reverts to a mode in which the user may remotely control execution of each experiment using the computer keyboard. In addition, the program runs some simple checks to see if the digital wave form synthesizer memory has been correctly loaded, and provides a binary address display that can be checked against the Array Controller panel to verify correct timing and operation of the Array Controller.

### **HARVEST1.BAS**

This program is used after all experiments (128 pulses) in a sequence have been completed and the Array Controller memory is full. The program allows the user to define a serial number for the raw spectral data file names so that they can be accessed by later programs. The raw spectral data are simply the voltages (8-bit) that were detected by each phototransistor at each ENCODE pulse during the experiment. In addition, three additional data vectors are appended to the spectral data, and these may include any 0.0

-> 2.0 volt signal that is generated during the experiment. In the case of this series of experiments, the servo motor position is detected optically and recorded at each ENCODE pulse in parallel with the diffraction spectrum data. The data files are in the form of 8-bit, comma-delimited integers. The files are designated RAWxxxxx.DAT, and are accessed by other programs for calculating sarcomere length and servo position as a function of time.

### **SPECNORM.BAS**

This program uses the geometrical setup data stored in TILT NORM.DAT and the spectral data from each experiment stored in RAWxxxxx.DAT to generate data files that contain sarcomere length and servo position as a function of time.

The sarcomere length is calculated for each time point as follows:

- 1- The location of the first order peak is determined by calculating the centroid of the intensity values for each phototransistor at each time point.
- 2- The geometry of the experimental setup (stored by TILT NORM.BAS) is used to determine the distance between the zero-order peak and the first-order diffraction peak.
- 3- The diffraction angle is calculated directly from the geometry of the experimental setup and the position of the first-order peak.
- 4- The sarcomere spacing is calculated from the grating equation for normal incidence:  $\sin(\theta) = m\lambda/a$  where:  
 $a$  = sarcomere length  
 $\lambda$  = laser wavelength  
 $m = 1$   
 $\theta$  = diffraction angle

The program then generates a two-column, comma-delimited file for each experiment, which consists of servo position and sarcomere length for 1024 time points.

## **DATAVIEW.BAS**

This program allows the servo position and sarcomere length versus time data files to be viewed graphically. Several filters are available to allow removal of noise in the signal. For example, a median rank 1 filter removes spurious "salt-and-pepper" noise from both the servo motor position and sarcomere length trace. A rolling average filter of variable rank is also available. Weak signals will cause the sarcomere length calculation algorithm to assign known default values to the sarcomere length. This amounts to an indication that no signal was detected at that time point. A window is defined within this program to clip out points that are known to be set to the no-signal default values. The program will then generate data files that can be easily used by standard graphics software to generate plots of the data.

## **IMAGEPRO.BAS**

This program uses the servo position and sarcomere length data files generated by SPECNORM.BAS to calculate the time delay between pulses as measured at two different points along the fiber. The program also uses the servo motor calibration curves to calculate the servo pulse amplitude. In addition, this program calculates the magnitude of the sarcomere length pulse and the sarcomere length baseline (sarcomere length before the application of the pulse).

The time delay for each pulse is calculated by cross correlating the servo pulse with the resulting sarcomere length pulse and determining the lag at which the maximum correlation occurs. The maximum correlation ( $r$ ) value, the signal strength (% of signal that is not set to the no-signal default value), the time lag at maximum correlation, servo and sarcomere pulse amplitudes are recorded in comma-delimited data files.

### **EXCELTAB.BAS**

This program uses the data files generated by IMAGEPRO.BAS to calculate the pulse propagation velocity and attenuation coefficient as described in the Methods section. Then, for each of the ten pulse types in each series of experiments (128 pulses total), the program tabulates the time delay between the two points that are sampled by the laser spot, the amplitude of the sarcomere length pulse at each of those two points, the propagation velocity, the attenuation coefficient, and the standard error for each of these values for all pulses of the same amplitude.

### **STPCORR.BAS**

This program will retrieve the raw diffraction spectrum data from optical disk and display the intensity of the 1° peak of the diffraction pattern vs. time, as well as the sarcomere length vs. time. The program will then make a data file to allow the results to be graphed using readily available graphics software. Using this program, it is possible to see the relationship between diffraction peak amplitudes and the steps and pauses in the sarcomere length pulse traces.

### **SPECANAL.BAS**

This program ran a series of checks on the raw spectral data to determine the characteristics of each diffraction spectrum prior to analysis. The program flags diffraction spectra with peak signal strength below the acceptable threshold, which was set to a digital value of 10. The program also searches for multiple diffraction peaks in the raw data. No multiple peaks were detected in any of the diffraction spectra. A second peak was defined as a local diffraction intensity maximum which was separated from the primary maximum by at least one phototransistor position, with a local minimum between the two peaks of at least 2 digital points below the peak of the second

maximum. The second peak signal was required to have a digital signal strength of at least 10 to be considered acceptable.

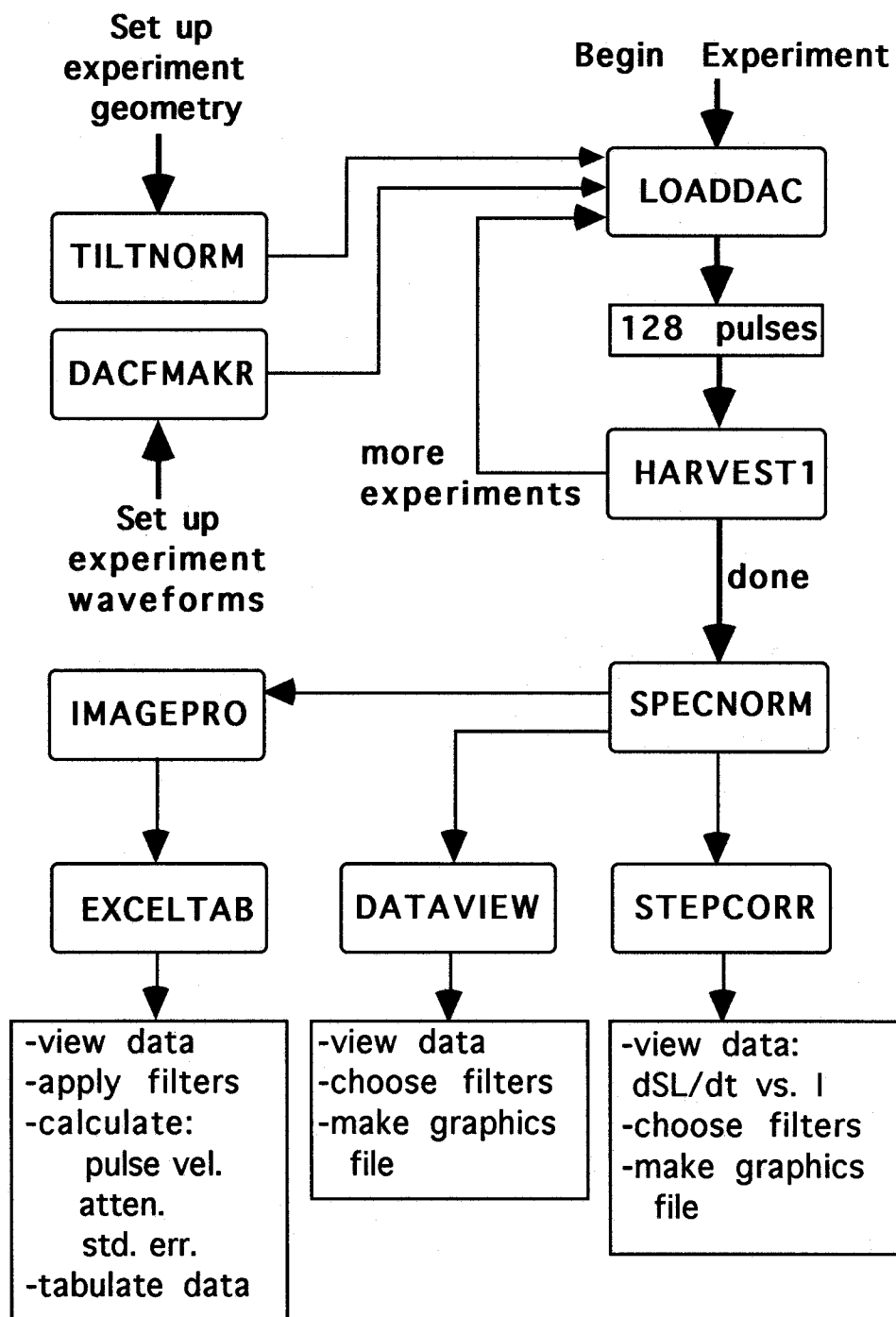


**Figure J.1.** Flow chart illustrating the use of the various programs for handling and viewing the data from each series of experiments. Heavy arrows indicate required steps.